Journal of Applied Physics

High thermoelectric power factor of *p*-type amorphous silicon thin films dispersed with ultrafine silicon nanocrystals

Cite as: J. Appl. Phys. **127**, 245304 (2020); https://doi.org/10.1063/5.0004318
Submitted: 14 February 2020 . Accepted: 03 June 2020 . Published Online: 26 June 2020

Ngan Hoang Pham, Örjan Vallin, J. Panda, M. Venkata Kamalakar, Junji Guo, Jun Luo, Chenyu Wen, Shi-Li Zhang, and Zhi-Bin Zhang

ARTICLES YOU MAY BE INTERESTED IN

Effect of thermal annealing on thermoelectric properties of $Bi_xSb_{2-x}Te_3$ thin films grown by sputtering
Journal of Applied Physics **127**, 245108 (2020); https://doi.org/10.1063/5.0002576

A first-principles prediction of an sp^3 carbon allotrope comprising four-, five-, six-, and eight-member rings
Journal of Applied Physics **127**, 245112 (2020); https://doi.org/10.1063/5.0004301

New horizons in thermoelectric materials: Correlated electrons, organic transport, machine learning, and more
Journal of Applied Physics **125**, 180902 (2019); https://doi.org/10.1063/1.5092525

© 2020 Author(s).

Journal of Applied Physics ARTICLE scitation.org/journal/jap

High thermoelectric power factor of *p*-type amorphous silicon thin films dispersed with ultrafine silicon nanocrystals

Cite as: J. Appl. Phys. **127**, 245304 (2020); doi: 10.1063/5.0004318
Submitted: 14 February 2020 · Accepted: 3 June 2020 ·
Published Online: 26 June 2020

View Online

Export Citation

CrossMark

Ngan Hoang Pham,[1] Örjan Vallin,[2] J. Panda,[3] M. Venkata Kamalakar,[3] Junji Guo,[4] Jun Luo,[5] Chenyu Wen,[1] Shi-Li Zhang,[1] and Zhi-Bin Zhang[1,a)]

AFFILIATIONS

[1]Division of Solid State Electronics, Department of Electrical Engineering, Uppsala University, 75121 Uppsala, Sweden
[2]The Ångström Microstructure Laboratory, Uppsala University, 75121 Uppsala, Sweden
[3]Department of Physics and Astronomy, Uppsala University, 75120 Uppsala, Sweden
[4]Key Laboratory of Microelectronic Devices and Integrated Technology, Institute of Microelectronics, Chinese Academy of Sciences, 100029 Beijing, China
[5]Institute of Microelectronics, Chinese Academy of Sciences, 100029 Beijing, China

[a)]**Author to whom correspondence should be addressed:** zhibin.zhang@angstrom.uu.se

ABSTRACT

Silicon, a candidate as an abundant-element thermoelectric material for low-temperature thermal energy scavenging applications, generally suffers from rather low thermoelectric efficiency. One viable solution to enhancing the efficiency is to boost the power factor (*PF*) of amorphous silicon (a-Si) while keeping the thermal conductivity sufficiently low. In this work, we report that $PF > 1\ \mathrm{m\,W m^{-1} K^{-2}}$ is achievable for boron-implanted *p*-type a-Si films dispersed with ultrafine crystals realized by annealing with temperatures ≤600 °C. Annealing at 550 °C initiates crystallization with sub-5-nm nanocrystals embedded in the a-Si matrix. The resultant thin films remain highly resistive and thus yield a low *PF*. Annealing at 600 °C approximately doubles the density of the sub-5-nm nanocrystals with a bimodal size distribution characteristic and accordingly reduces the fraction of the amorphous phase in the films. Consequently, a dramatically enhanced electrical conductivity up to 10^4 S/m and hence $PF > 1\ \mathrm{m\,W m^{-1} K^{-2}}$ measured at room temperature are achieved. The results show the great potential of silicon in large-scale thermoelectric applications and establish a route toward high-performance energy harvesting and cooling based on silicon thermoelectrics.

© *2020 Author(s). All article content, except where otherwise noted, is licensed under a Creative Commons Attribution (CC BY) license (http://creativecommons.org/licenses/by/4.0/).* https://doi.org/10.1063/5.0004318

INTRODUCTION

A thermoelectric generator (TEG) represents a unique device to directly convert waste heat into electricity. Advances in miniaturization and integration of electronic circuits for Internet of Things (IoT) call for solutions to mobile, and distributed and renewable power sources and TEG appear to be an attractive alternative.[1–3] This application requires thermoelectric materials operating in low temperature range around room temperature (RT) with bismuth telluride as the main candidate so far.[4–6] The anticipated broad applications of TEG require innovations to address two major issues. One is the persistently poor conversion efficiency, which is primarily characterized by the dimensionless figure of merit $ZT = (\sigma S^2/\kappa)T$, where σ, S, κ, and T represent the electrical conductivity, the Seebeck coefficient, the thermal conductivity, and the absolute operating temperature, respectively. The other issue is associated with the use of rare and toxic tellurides, e.g., Bi_2Te_3 and PbTe, for their unprecedented TE performance in the low temperature regime below 400 °C; in bulk form, they typically deliver a ZT value close to 1 at RT. For sustainable development and wide applications, the selection of abundant and environmentally benign

© Author(s) 2020

materials coupled with the consideration of low-cost production is of paramount importance. Silicon is the second most abundant element in the Earth's crust and has been the base material in the modern microelectronics industry. However, single crystalline silicon (sc-Si) suffers from a rather low ZT around 0.01 due to its large bulk thermal conductivity (~150 $\mathrm{W m^{-1} K^{-1}}$).[7,8] An efficient strategy to enhance ZT of sc-Si is suppressing its thermal conductivity by nanostructuring in the form of, e.g., superlattice, nanowires, and nano-meshes of sc-Si, which generally involves demanding and complicated processing.[9,10]

In general, a too low value of κ is not beneficial to maximizing output power in a specific TEG and a too high value reduces temperature gradient (ΔT) across thermoelectric (TE) legs. The latter causes a degradation of the TEG conversion efficiency. Therefore, it is necessary to prioritize the increase of power factor ($PF = S^2\sigma$)[11,12] as long as κ is reasonably low. Recently, it becomes an attractive solution to engineer amorphous silicon (a-Si) thin films using standard silicon technology to obtain high PF silicon.[13] To construct a TEG, n- and p-type constituents of equal performance are crucial. We have obtained a PF of ~3.4 $\mathrm{m W m^{-1} K^{-2}}$ at RT using arsenic-doped n-type a-Si thin films processed at ~500 °C.[13] For p-type Si, a $PF > 1$ $\mathrm{m W m^{-1} K^{-2}}$ has been reported for boron-doped Si thin films which have been treated at rather a high temperature (1000 °C for hours) for the recovery of implantation damages and for dopant activation.[11] It has been well known that the crystallization of a-Si is very sensitive to annealing temperature and duration.[14] The conditions with elevated temperatures (e.g., >650 °C) and extended duration (i.e., hours) often lead to crystals of hundred nanometers to micrometer in size.[15,16] Si thin films with large-crystal-size Si crystals are expected to have high thermal conductivity and thus lower ZT. As a TEG requires both n- and p-type thermoelectric legs of similar efficiency, it is important to explore temperature process windows for boosting PF of p-type TE silicon thin films with sufficient low κ.[17–21]

In response to this challenge, this work studies the TE transport properties of boron-implanted p-type a-Si thin films dispersed with ultrafine nanocrystals realized by limiting the process temperature in the range of 450–600 °C. The result reveals a precise process window that favors the formation of desired sub-5-nm nanocrystals, which results in a high electrical conductivity of up to 10^4 S/m and high PF to ~2 $\mathrm{m W m^{-1} K^{-2}}$ at RT. As thin films consisting of ultrafine nanocrystals possess very low κ due to efficient phonon scattering at grain boundaries,[11] our study provides a solution to achieve high performance p-type thermoelectric silicon thin films, in combination of the n-type counterpart, for the applications of inexpensive and distributed thermal energy harvesting and cooling operating in a low temperature range.

EXPERIMENTS

The parent a-Si thin films were deposited on top of thermally oxidized p-type sc-Si wafers with a 300 nm thick oxide (SiO_2) layer. The a-Si thin films were deposited in a low pressure chemical vapor deposition (LPCVD) reactor with 45 standard cubic centimeter per minute (sccm) silane, at 0.2 Torr pressure and 560 °C. The deposition rate was 2.6 nm/min. The nominal thickness of a-Si films was 100 nm at which phonon scattering at surfaces/interfaces may play a role in reducing the thermal conductivity.[13] Boron ion implantation was conducted at RT to obtain four different nominal dopant concentrations, i.e., $C_B = 10^{18}$, 10^{19}, 10^{20}, and 10^{21} $\mathrm{cm^{-3}}$. For each nominal concentration, energies of 30, 50, 100, and 160 keV were used in order to achieve a uniform dopant distribution in the thin films. The energies and the doses were selected according to the calculation by using Stopping and Range of Ions in Matter (SRIM) simulation (not shown here) for the ion implantation. Electrical activation of the boron dopants was carried out by rapid thermal processing (RTP) in a nitrogen atmosphere at various temperatures T_a from 450 to 600 °C for 10 min with a step of 50 °C. The temperature was well controlled during the rapid thermal annealing. The morphology of the best performing film was studied by means of high resolution transmission electron microscopy (HRTEM) on a FEI Tecnai G2 UT instrument with a field emission gun operated at 200 kV and a point resolution of 0.19 nm.

The microstructural properties of the thin films were characterized by Raman resonance spectroscopy (RRS) and glancing incident x-ray diffractometry (GR-XRD). The RRS measurements were performed using the Renishaw inVia system with the 532 nm laser at room temperature. Electrical sheet resistance was measured in darkness on test samples with a van der Pauw geometry using Keysight B1500A semiconductor parameter analyzer at room temperature (Fig. S1 in the supplementary material). The Hall measurement was conducted using a home-built system consisting of an electrical magnet, a Keithley 2400 source meter, a Keithley 2182A nanovolmeter, and a Lakeshore 455 DSP Gauss meter. For the measurement of the Seebeck coefficient, test structures comprising electrodes of Ti/Au for heating, temperature sensing, and electrical measurement were fabricated (Fig. S2 in the supplementary material). Details regarding the test sample fabrication and Seebeck coefficient measurement can be found in the supplementary material.

RESULTS AND DISCUSSION

The amorphous nature of an as-deposited Si thin film was confirmed by XRD and Raman as described in our previous work.[13] The subsequent boron implantation is expected to induce damages to the thin films. The annealing process is meant for improving electrical transport properties of the materials, which usually requires rather a high temperature at 1000 °C.[22] As our samples were annealed at temperature $T_a \leq 600$ °C, the ion bombardment-associated damages most likely remain in the thin film. We found that annealing at temperatures below 500 °C did not change the amorphous nature as evidenced by XRD analysis (not shown here), and the samples remained highly resistive with their sheet resistance out of the measurement range of our instrument. Therefore, the discussion below focuses on the samples annealed at 550 and 600 °C. As the XRD data shown in Fig. 1(a), the Si thin films with low boron concentrations (i.e., $C_B = 10^{18}$ and 10^{19} $\mathrm{cm^{-3}}$) and annealed at $T_a = 550$ °C persistently stay in the amorphous state. By increasing the boron concentration to 10^{20} $\mathrm{cm^{-3}}$, two well-established diffraction peaks assigned to Si (111) and (220) appear. The peaks become very weak when the boron concentration is further increased to 10^{21} $\mathrm{cm^{-3}}$. On the

© Author(s) 2020

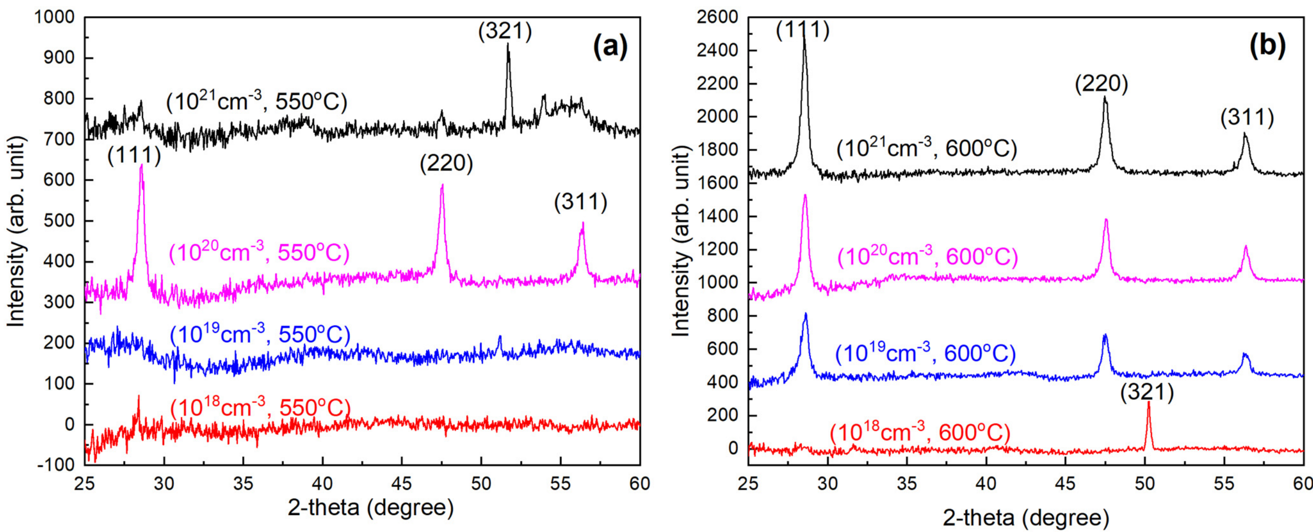

FIG. 1. XRD patterns of the boron-implanted a-Si thin films with different nominal boron concentrations after annealing at (a) $T_a = 550$ and (b) 600 °C. The XRD index was inferred from Refs. 22 and 23.[47,48]

other hand, for $T_a = 600$ °C, as displayed in Fig. 1(b), the crystallization tends to occur at lower boron concentration. One can see that the crystallinity feature appears similar between 550 and 600 °C when $C_B = 10^{20}$ cm^{-3}.

Raman resonance spectroscopy provides a powerful means to investigate crystals of ultra-fine sizes as the atomic vibration modes are sensitive to grain size.[13–25] As shown in Fig. 2, a broad Gaussian peak at ∼480 cm^{-1} attributed to a-Si[26] is visible, particularly in the samples with high boron concentrations of 10^{20} and 10^{21} cm^{-3}. All the samples under investigation possess an asymmetric Lorentzian signal at ∼516–518 cm^{-1}. As the Raman peak from crystalline Si appears at 520.5 cm^{-1}, the peaks at ∼516–518 cm^{-1} can be ascribed to a peak shift caused by the reduction of crystal size to the nanometer scale.[23,27,28] They correspond to the transverse optical (TO) phonon peaks, are asymmetrically broadened toward the low energy side, and exhibit characteristics of a Fano line shape.[24,27] Note that an additional signal at ∼508–510 cm^{-1} and further down to 503 cm^{-1} appears in the Raman patterns of the samples with 10^{19} and 10^{20} cm^{-3} boron concentration and annealed at 600 °C, which can be presumably ascribed to the presence of ultrafine nanocrystals or ordering domains. This signal was previously observed by other research groups and assumed to be the effect of grain boundaries.[29–31]

From the degree of peak shift with respect to the sc-Si peak (520.5 cm^{-1}), the size of nanocrystals can be estimated according to the following relationship:[25]

$$\Delta\omega(D) = \frac{120.8}{\frac{a}{D} + 0.53}\left(\frac{a}{D}\right)^2, \quad (1)$$

where D is the diameter of a nanocrystal, a the lattice parameter for Si ($a = 0.543$ nm), and $\Delta\omega(D)$ the Raman frequency shift associated with the size reduction. The volumetric fraction of the crystalline phase, χ_c, can be obtained by considering the ratio of peak intensity for the amorphous phase (480 cm^{-1}) to that for the crystalline phase (∼510–520 cm^{-1}) according to

$$\chi_c = \frac{I_c}{I_c + I_a}, \quad (2)$$

where I_c and I_a are the peak areas for the crystalline and amorphous Si, respectively. Corrections need to be considered by subtracting the peak intensity contributed by the underlying Si substrate.[23,26] For the calculation of grain size and degree of crystallization, each Raman peak was deconvoluted into three components corresponding to amorphous, bimodal nanocrystalline (∼516–518 cm^{-1} and ∼503–510 cm^{-1}), and crystalline (520.5 cm^{-1}) [see an example in Fig. 2(b)]. The calculation results indicate that the peak at ∼516–518 cm^{-1} corresponds to a grain size of 4–5 nm, while the peak at ∼503–510 cm^{-1} to the size of 1–2 nm. As shown in Table I, annealing the samples with a boron concentration of 10^{18}, 10^{19}, and 10^{21} cm^{-3} at 550 °C gives rise to nanocrystals of 4–5 nm in size with ∼36% crystallization degree. For $C_B = 10^{20}$ cm^{-3}, the Si thin film exhibits an increased crystallization degree, i.e., ∼69%, with the grain size reduced to ∼3 nm. By increasing T_a to 600 °C, the grain size of nanocrystals is decreased to 3–4 nm while the fraction of a-Si drops rapidly and becomes undetectable for $C_B = 10^{20}$ and 10^{21} cm^{-3}. Interestingly, finer crystals with the size of 1–2 nm appear and coexist with the larger crystals as indicated by the double peaks in the Raman spectra (Fig. 2). As boron can effectively enhance the crystallization rate in a-Si,[14,32] the presence of boron atoms facilitates the formation and growth of the ordered domains in the amorphous phase. A higher boron concentration leads, in general, to smaller crystal size under the same

© Author(s) 2020

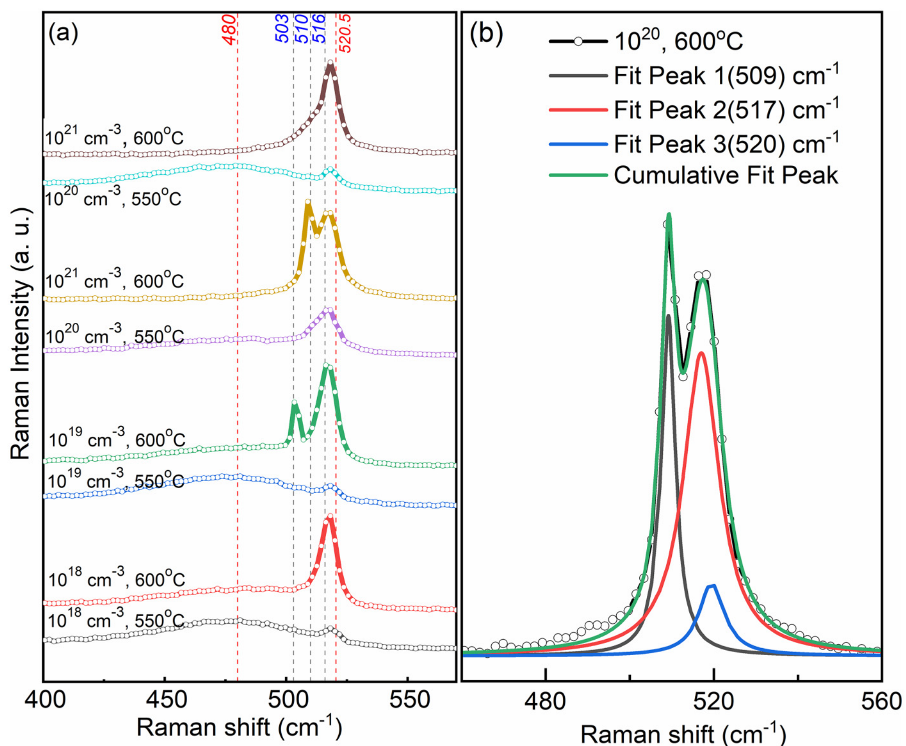

FIG. 2. (a) Raman spectrum of samples after annealing at temperatures 550 and 600 °C. (b) A typical Raman spectrum of sample (10^{20} cm^{-3}, 600 °C) for crystalline size analysis where the measured peaks are deconvoluted into nanocrystalline peak (508.8 cm^{-1}), nanocrystalline peak (516.9 cm^{-1}), and crystalline peak (520.5 cm^{-1}).

annealing conditions. Bimodal grain size distribution for B-doped Si nanocrystals has also been reported for samples annealed at 800 °C.[33,34]

The electrical conductivity σ is found to strongly depend on C_B and T_a. At $C_B = 10^{18}$ cm^{-3}, all the a-Si thin films, after annealed at 450–600 °C, remain non-conductive. At higher C_B, σ generally increases with T_a as shown in Fig. 3. Remarkably, σ jumps up by 2–3 orders of magnitude and reaches $(1.5 \pm 0.1) \times 10^4$ and $(3.7 \pm 0.1) \times 10^4$ S/m for $C_B = 10^{20}$ and 10^{21} cm^{-3}, respectively, when T_a is raised from 550 to 600 °C. The Hall measurement reveals that the annealing at 600 °C leads to hole mobility (μ_H) of 26 ± 2 and 23 ± 2 cm^2 V^{-1} s^{-1} and a hole concentration of 5.2×10^{19} and 1.6×10^{20} cm^{-3} for the samples with $C_B = 10^{20}$ and 10^{21} cm^{-3}, respectively. It has been previously revealed that implanted boron atoms dramatically enhance the crystallization of a-Si annealed at a temperature as low as 500 °C[32] and can be effectively electrically activated already at 550 °C.[35] The activated boron atoms are bonded with silicon atoms in re-ordered domains, donating holes to increase the carrier concentration, and thus to enhance the electrical conductivity. In our samples, the boron-doped Si thin films can be visualized as nanocrystals embedded in the amorphous phase after appropriate annealing. As seen in Table I, the rapid reduction in the fraction of the amorphous phase and crystallization with bimodal size distribution occurs when T_a is raised from 550 to 600 °C. These changes effectively shorten the inter-distance between the nanocrystals, leading to enhanced electrical conductance. Compared to the single grain size distribution (i.e., ~4–5 nm in the case of $T_a = 550$ °C), a much larger inter-grain contact area is expected with the bimodal grain size distribution as the smaller ones (~1–2 nm) replace most the amorphous phase in the network of the larger grains (~3–4 nm). Previous studies appear to suggest that the crystallization process recombines the dangling bonds and passivates defects, both of which would improve electronic transport.[14,36]

The measurement of Seebeck coefficient S yields 356 ± 2 and 177 ± 1 μV K^{-1} for the samples with $C_B = 10^{20}$ and 10^{21} cm^{-3}, respectively, both were annealed at $T_a = 600$ °C. They are lower than

TABLE I. Crystallinity of the annealed samples extracted from the Raman analysis where the sample identification refers to the boron concentration/annealing temperature.

Samples (cm^{-3}/°C)	Fraction of amorphous phase (%)	Crystal size (nm)/ corresponding fraction (%)
10^{18}/550	64.4	4.6/35.6
10^{19}/550	63.9	4.2/36.1
10^{20}/550	31.2	3.3/68.8
10^{21}/550	57.7	4.2/42.3
10^{18}/600	24.8	4.0/75.2
10^{19}/600	12.5	3.6/52.0; 1.5/35.5
10^{20}/600	0	3.9/42.5; 2.0/57.5
10^{21}/600	0	4.2/62.5; 2.4/37.5

© Author(s) 2020

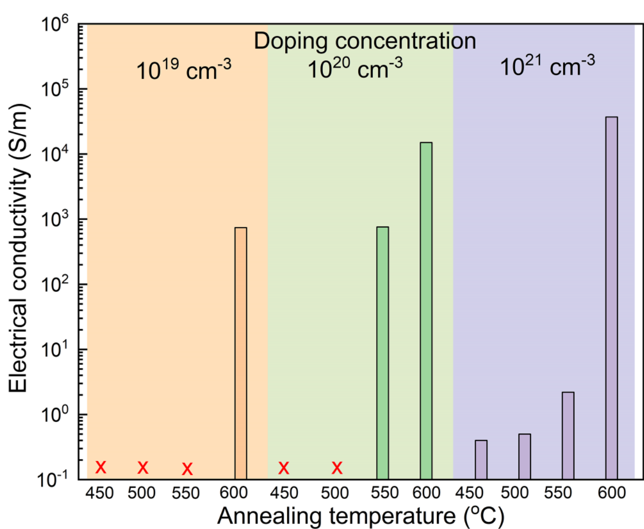

FIG. 3. Electrical conductivity in log scale at various boron concentrations and annealing temperatures. The data points that are out of measurement range are marked by cross symbol.

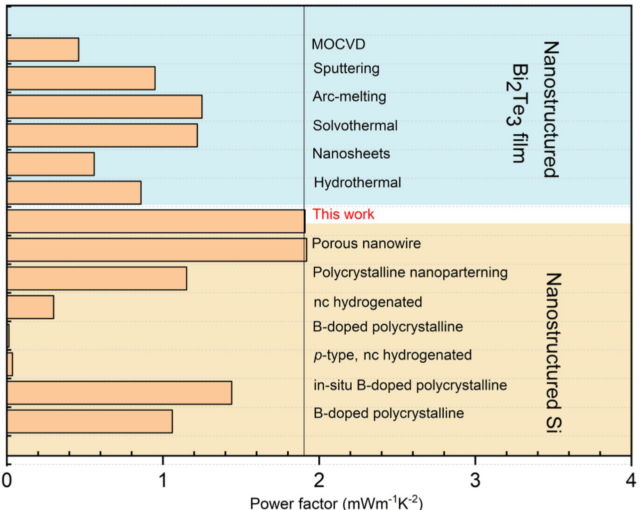

FIG. 4. Comparison of power factor between this work and the state of the art *p*-type Si-based and Bi_2Te_3 thermoelectric thin films. References: MOCVD (metalorganic chemical vapor deposition),[47] sputtering (Bi_2Te_3 on polyimide substrate),[48] arc-melting (to form nanostructured Bi_2Te_3),[49] solvothermal,[50] nanosheets (for assembled of Bi_2Te_3),[51] hydrothermal,[52] porous nanowire (Si arrays),[53] polycrystalline nanopatterning (of Si film with phononic crystal),[54] nc hydrogenated (B-doped Si),[44] B-doped polycrystalline Si,[39] p-type, nc hydrogenated Si,[55] *in situ* B-doped polycrystalline Si film,[56] B-doped polycryslline Si film,[22] and B-doped nanocrystalline Si.[11]

that of boron-doped sc-Si (~500 μVK^{-1}), with a carrier concentration of 1.5×10^{19}. The sample with $C_B = 10^{20}$ cm^{-3} has lower σ but larger S than those of $C_B = 10^{21}$ cm^{-3}, which follows the Pisarenko formula, i.e., $S \propto \frac{K}{e}\ln(\sigma)$,[37,38] where K and e are the Boltzmann constant and the electronic charge, respectively, and the similar result has also been observed in highly doped polycrystalline Si with a similar doping concentration.[39] When we compare the samples of the same $C_B = 10^{20}$ cm^{-3} annealed at different temperatures, S of 550 °C ($220 \pm 9\,\mu$VK^{-1}) is lower than that of 600 °C ($356 \pm 2\,\mu$VK^{-1}), which cannot be explained by using the Pisarenko theory as the former has lower electrical conductivity ($\sigma = 760$ S/m). This contradiction indicates that energy filtering might come in to play in the sample with $C_B = 10^{20}$ cm^{-3} annealed at 600 °C to increase its Seebeck coefficient. As for the sample with $C_B = 10^{21}$ cm^{-3} annealed at 600 °C having the highest hole concentration, the Pisarenko mechanism dominates and thus leads to a low Seebeck coefficient of $177 \pm 1\,\mu$V K^{-1}. Using the aforementioned σ (=1.5×10^4 S/m), *PF* of the sample with $C_B = 10^{20}$ cm^{-3} annealed at 600 °C is calculated to be 1.9 m Wm^{-1} K^{-2}. In comparison to the state of the art in *p*-type Si TE thin films near the room temperature range (Fig. 4), our process with a-Si films doped with boron and annealed at low temperatures shows excellent advantages with respect to the TE power factor, manufacturability, and scalability. In addition, the obtained *PF* surpasses those offered by nanostructured Bi_2Te_3 thin films. Although these thermoelectric materials have different thermal conductivities, a higher power factor of a thermoelectric material is more relevant to the output power of TEGs as mentioned earlier. It is noticed that annealing of a-Si at temperatures beyond 600 °C and/or extended duration to many hours is expected to crystallize the a-Si with relatively large grain sizes[14] which may lead to electrical and thermal conductivities close to that of sc-Si.[40]

It is possible to estimate the value of thermal conductivity. The total thermal conductivity κ is the sum of the lattice and electrical thermal conductivity components denoted as κ_l and κ_e, respectively. κ_e can be calculated using the Wiedemann–Franz law,

$$\kappa_e = \sigma \cdot \pi^2 k_B^2 T/3e^2, \tag{3}$$

where e is the electron charge and k_B is the Boltzmann constant.[41] Taking the measured σ of the sample with $C_B = 10^{20}$ cm^{-3} annealed at 600 °C, κ_e ~0.2 Wm^{-1} K^{-1} is obtained. The lattice thermal conductivity of nanocrystalline materials can be calculated based on a model proposed by Dong *et al.*,[42]

$$\kappa_l = \frac{\kappa_0 \Big/ \left(1 + \dfrac{l_0}{D^\alpha}\right)}{1 + R_k[\kappa_0/(1 + l_0/D^\alpha)]/D}, \tag{4}$$

where κ_o is the single crystal thermal conductivity, l_o the single crystal phonon mean free path (nm), D the grain size (nm), α an affirmatory exponent ranging between ½ and ¾, and R_k the Kapitza resistance (m^2 KW^{-1}). With a crystal size smaller than 10 nm, κ_l was computed[11,39] to be less than 10 Wm^{-1} K^{-1}. Experimental measurements of κ for non-doped nanocrystalline Si with a nanocrystal size of ~64 nm also yielded a value below 10 Wm^{-1} K^{-1}.[43] Similar values of κ (3.2 and 1.5 Wm^{-1} K^{-1} for as-grown and annealed samples at 500 °C, respectively) have also

© Author(s) 2020

been obtained in microcrystalline p-type silicon.[44] By assuming κ of $10\,\mathrm{W\,m^{-1}\,K^{-1}}$, which is reasonably the upper limit for the thermal conductivity of all the samples under investigation, room-temperature ZT of the sample with $C_B = 10^{20}\,\mathrm{cm^{-3}}$ annealed at 550 °C is low at around 10^{-3}. The value increases to ∼0.06 for the sample with $C_B = 10^{20}\,\mathrm{cm^{-3}}$ and annealed at 600 °C and to ∼0.04 for the sample with $C_B = 10^{21}\,\mathrm{cm^{-3}}$ and annealed at 600 °C. The persistent low ZT values, to a large degree, are mainly due to their small Seebeck coefficient.

CONCLUSION

We have demonstrated a low-temperature process window for achieving thermoelectric power factor $\sim 2\,\mathrm{m\,W\,m^{-1}\,K^{-2}}$ for p-type a-Si thin films dispersed with sub-5-nm nanocrystals. By varying the boron concentration and annealing temperature, a several-order-of-magnitude increase in the electrical conductivity has been obtained. Our study of the structural and transport properties of boron doped p-type a-Si thin films reveals that the substantial enhancement in the electrical conductivity is correlated with the doubling in the density and the emergence of the bimodal characteristic of the sub-5-nm crystals in the a-Si thin films. The bimodal nanocrystals favor a close packing which can maximize the inter-nanocrystals electrical contact and thus increase the electrical conductivity of the thin films. As thin films of ultrafine nanocrystals have low thermal conductivity, our results pave the way toward the improvement of the thermoelectric properties of silicon for developing silicon-based thermoelectric devices.

SUPPLEMENTARY MATERIAL

See the supplementary material for test structure and method for electrical, thermoelectric measurements.

ACKNOWLEDGMENTS

The authors would like to acknowledge Professor Anders Hallén for SIMS simulation, Dr. Lars Riekehr for help with TEM inspection, Dr. Debashree Banerjee (CSIR-Central Electronics Engineering Research Institute in India), and Dr. Kabir Majid Samani (Department of Microtechnology and Nanoscience, Chalmers University of Technology) for useful discussion on experimental work. We also thank Dr. Tomas Nyberg for his help with Hall measurement equipment. This work was supported by the Swedish Research Council (Nos. 621-2014-5596 and 2016-03278).

DATA AVAILABILITY

The data that support the findings of this study are available from the corresponding author upon reasonable request.

REFERENCES

[1] D. Beretta, N. Neophytou, J. M. Hodges, M. G. Kanatzidis, D. Narducci, M. Martin- Gonzalez, M. Beekman, B. Balke, G. Cerretti, W. Tremel, A. Zevalkink, A. I. Hofmann, C. Müller, B. Dörling, M. Campoy-Quiles, and M. Caironi, Mater. Sci. Eng. R **138**, 210 (2018).
[2] M. Haras and T. Skotnicki, Nano Energy **54**, 461 (2018).
[3] J. P. Heremans, M. S. Dresselhaus, L. E. Bell, and D. T. Morelli, Nat. Nanotechnol. **8**, 471 (2013).
[4] Z.-G. Chen, G. Han, L. Yang, L. Cheng, and J. Zou, Prog. Mater. Sci. Mater. Int. **22**, 535 (2012).
[5] C. Gayner and K. K. Kar, Prog. Mater. Sci. **83**, 330 (2016).
[6] J.-F. Li, W.-S. Liu, L.-D. Zhao, and M. Zhou, NPG Asia Mater. **2**, 152 (2010).
[7] L. Weber and E. Gmelin, Appl. Phys. A **53**, 136 (1991).
[8] S. K. Bux, R. G. Blair, P. K. Gogna, H. Lee, G. Chen, M. S. Dresselhaus, R. B. Kaner, and J.-P. Fleurial, Adv. Funct. Mater. **19**, 2445 (2009).
[9] B. Sun, M. Shao, and S. Lee, Adv. Mater. **28**, 10539 (2016).
[10] D. Narducci, L. Belsito, and A. Morata, in *Advanced Micro and Nanosystems*, edited by D. Dávila Pineda and A. Rezania (Wiley-VCH Verlag GmbH & Co. KGaA, Weinheim, 2017), pp. 55–91.
[11] N. Neophytou, X. Zianni, H. Kosina, S. Frabboni, B. Lorenzi, and D. Narducci, Nanotechnology **24**, 205402 (2013).
[12] D. Narducci, Appl. Phys. Lett. **99**, 102104 (2011).
[13] D. Banerjee, Ö Vallin, K. M. Samani, S. Majee, S.-L. Zhang, J. Liu, and Z.-B. Zhang, Nano Energy **44**, 89 (2018).
[14] C. Spinella, S. Lombardo, and F. Priolo, J. Appl. Phys. **84**, 5383 (1998).
[15] M. K. Hatalis and D. W. Greve, J. Appl. Phys. **63**, 2260 (1988).
[16] R. Kakkad, J. Smith, W. S. Lau, S. J. Fonash, and R. Kerns, J. Appl. Phys. **65**, 2069 (1989).
[17] G. J. Snyder, J. R. Lim, C.-K. Huang, and J.-P. Fleurial, Nat. Mater. **2**, 528 (2003).
[18] T. Huesgen, P. Woias, and N. Kockmann, Sens. Actuators A Phys. **145–146**, 423 (2008).
[19] M. Strasser, R. Aigner, M. Franosch, and G. Wachutka, Sens. Actuators A Phys. **97–98**, 535 (2002).
[20] A. P. Perez-Marín, A. F. Lopeandía, L. l. Abad, P. Ferrando-Villaba, G. Garcia, A. M. Lopez, F. X. Muñoz-Pascual, and J. Rodríguez-Viejo, Nano Energy **4**, 73 (2014).
[21] J. Xie, C. Lee, and H. Feng, J. Microelectromech. Syst. **19**, 317 (2010).
[22] J. Xie, C. Lee, M.-F. Wang, Y. Liu, and H. Feng, J. Micromech. Microeng. **19**, 125029 (2009).
[23] S. V. Gaisler, O. I. Semenova, R. G. Sharafutdinov, and B. A. Kolesov, Phys. Solid State **46**, 1528 (2004).
[24] N. H. Nickel, P. Lengsfeld, and I. Sieber, Phys. Rev. B **61**, 15558 (2000).
[25] W. Ke, X. Feng, and Y. Huang, J. Appl. Phys. **109**, 083526 (2011).
[26] T. Kamei, P. Stradins, and A. Matsuda, Appl. Phys. Lett. **74**, 1707 (1999).
[27] E. G. Barbagiovanni, D. J. Lockwood, P. J. Simpson, and L. V. Goncharova, Appl. Phys. Rev. **1**, 011302 (2014).
[28] C. M. Hessel, J. Wei, D. Reid, H. Fujii, M. C. Downer, and B. A. Korgel, J. Phys. Chem. Lett. **3**, 1089 (2012).
[29] G. Xiao-Yong, Z. Jian-Tao, L. Yu-Fen, L. Qing-Geng, C. Yong-Sheng, G. Jin-Hua, Y. Shi-E, and L. Jing-Xiao, Acta Phys. Pol. A **115**, 738 (2009).
[30] B. P. Swain, S. Afr. J. Sci. **4**, 77 (2009).
[31] Q. Wang, Y. Zhang, R. Hu, D. Ge, and N. Ren, J. Appl. Phys. **114**, 183504 (2013).
[32] L. Csepregi, E. F. Kennedy, T. J. Gallagher, J. W. Mayer, and T. W. Sigmon, J. Appl. Phys. **48**, 4234 (1977).
[33] C. Song, J. Xu, G. Chen, H. Sun, Y. Liu, W. Li, L. Xu, Z. Ma, and K. Chen, Appl. Surf. Sci. **257**, 1337 (2010).
[34] C. Song, J. Xu, Q. Wang, G. Zha, W. Li, and K. Chen, Solid State Commun. **151**, 697 (2011).
[35] M. Y. Tsai and B. G. Streetman, J. Appl. Phys. **50**, 183 (1979).
[36] J. C. McCallum, in *The 11th Australian Conference on Nuclear Techniques of Analysis and the 5th Vacuum Society of Australia Congress* (Australian Institute of Nuclear Science and Engineering, 1999), pp. 232–235.
[37] H. Wu, C. Chang, D. Feng, Y. Xiao, X. Zhang, Y. Pei, L. Zheng, D. Wu, S. Gong, Y. Chen, J. He, M. G. Kanatzidis, and L.-D. Zhao, Energy Environ. Sci. **8**, 3298 (2015).
[38] J. P. Heremans, V. Jovovic, E. S. Toberer, A. Saramat, K. Kurosaki, A. Charoenphakdee, S. Yamanaka, and G. J. Snyder, Science **321**, 554 (2008).

© Author(s) 2020

[39]K. Valalaki, N. Vouroutzis, and A. G. Nassiopoulou, J. Phys. D Appl. Phys. **49**, 315104 (2016).
[40]J. D. Plummer, M. D. Deal, and P. B. Griffin, *Silicon VLSI Technology: Fundamentals, Practice and Modeling* (Prentice Hall, 2000).
[41]A. D. McConnell, S. Uma, and K. E. Goodson, J. Microelectromech. Syst. **10**, 360 (2001).
[42]H. Dong, B. Wen, and R. Melnik, Sci. Rep. **4**, 7037 (2015).
[43]Z. Wang, J. E. Alaniz, W. Jang, J. E. Garay, and C. Dames, Nano Lett. **11**, 2206 (2011).
[44]E. Acosta, V. Smirnov, P. S. B. Szabo, J. Buckman, and N. S. Bennett, J. Electron. Mater. **48**, 2085 (2019).
[45]Q. Shabir, A. Pokale, A. Loni, D. R. Johnson, L. T. Canham, R. Fenollosa, M. Tymczenko, I. Rodríguez, F. Meseguer, A. Cros, and A. Cantarero, Silicon **3**, 173 (2011).
[46]S. Fujii, S.-I. Kuroki, X. Zhu, M. Numata, K. Kotani, and T. Ito, ECS Trans. **16**, 145 (2008).
[47]A. Giani, F. Pascal-Delannoy, A. Boyer, A. Foucaran, M. Gschwind, and P. Ancey, Thin Solid Films **303**, 1 (1997).
[48]P. Nuthongkum, R. Sakdanuphab, M. Horprathum, and A. Sakulkalavek, J. Electron Mater. **46**, 6444 (2017).
[49]M. Gharsallah, F. Serrano-Sánchez, J. Bermúdez, N. M. Nemes, J. L. Martínez, F. Elhalouani, and J. A. Alonso, Nanoscale Res. Lett. **11**, 142 (2016).
[50]L. Yang, Z.-G. Chen, M. Hong, G. Han, and J. Zou, ACS Appl. Mater. Interfaces **7**, 23694 (2015). 2
[51]W. Guo, J. Ma, and W. Zheng, J. Alloys Compd. **659**, 170 (2016).
[52]J. Fu, S. Song, X. Zhang, F. Cao, L. Zhou, X. Li, and H. Zhang, Cryst. Eng. Commun. **14**, 2159 (2012).
[53]T. Zhang, S. Wu, X. Ju, Z. Ruiting, and C. Guoan, Nano Energy **13**, 433 (2015).
[54]M. Nomura, Y. Kage, D. Müller, D. Moser, and O. Paul, Appl. Phys. Lett. **106**, 223106 (2015).
[55]J. Loureiro, T. Mateus, S. Filonovich, M. Ferreira, J. Figueira, A. Rodrigues, B. F. Donovan, P. E. Hopkins, and I. Ferreira, Appl. Phys. A **120**, 1497 (2015).
[56]D. Moser, D. Ilkaya, D. Kopp, and O. Paul, *2012 IEEE Sensors* (IEEE, Taipei, 2012), pp. 1–4.

© Author(s) 2020